MJO and CCEW modulation on South China Sea and Maritime Continent boreal winter subseasonal peak precipitation

Wayne Yuan-Huai Tsai, Mong-Ming Lu [*], Chung-Hsiung Sui, and Po-Hsiung Lin

Department of Atmospheric Science, National Taiwan University, Taipei City, Taiwan

ABSTRACT

Rainfall over South China Sea (SCS)-Maritime Continent (MC) region involves multiple-scale phenomena such as the annual cycle, monsoon variability, ENSO, Madden-Julian Oscillation (MJO), and convectively coupled equatorial waves (CCE-Ws). This study focuses on documenting MJO and CCEW modulation on the boreal winter subseasonal peak precipitation, which is an event with maximum 15-day accumulated rainfall amount during November to February, summarized at 10 by 10 degrees of longitude and latitude box areas in the region. It turns out that MJO shows strong influence on the peak event occurrence time. However, MJO has almost no positive effect on the peak event in the near equator land area. Mixed Rossby-gravity wave and tropical disturbance (MT) and equatorial Rossby (ER) wave show strong positive modulation on peak rainfall mean intensity. Cases during the SCS Two Island Monsoon Experiment (SCSTIMX) winters (2016/17 and 2017/18) are analyzed. To the north of 5°N, the peak event in 2016/17 occurred concurrently with MJO convective phase, while in 2017/18 as lack of MJO activity the occurrence time was modulated by the ER wave. The 2016/17 peak event shows weaker mean rainfall intensity than the 2017/18 event. To the south of 5°N, the area-mean peak event occurrence time was delayed in 2016/17, while the intensity was enhanced by the joint modulation of MJO, Kelvin and ER waves. The importance of understanding the area-mean and within-area-difference of peak rainfall events in the SCS-MC region was discussed. The findings can be applied to assess the subseasonal predictability of dynamical forecast models.

1. INTRODUCTION

The South China Sea (SCS) and its surrounding Maritime Continent (MC) is one of the wettest region in the Tropics particularly during the boreal winter months. SCS-MC covers South China Sea and Philippine Sea including Vietnam, Philippine, and 25000 equatorial islands extended from Sumatra to Papua New Guinea (around 90 - 150°E) (See YMC website http://www.jamstec.go.jp/ymc/ymc_about.html; Ling et al. 2017). Convection in this wet and warm region can be influenced by the dynamical systems of various scales such as the diurnal cycle (Yang and Slingo 2001; Kikuchi and Wang 2008; Qian 2008), synoptic scale monsoonal surges and vortexes (Chang et al. 2005a, b; Robertson et al. 2011; Chen et al. 2015a; Nguyen et al. 2016; Lim et al. 2017),

intraseasonal oscillations/MJO (Peatman et al. 2014; Vincent and Lane 2016; Hung and Sui 2018); convectively coupled waves (Liebmann and Hendon 1990); ENSO (Haylock and McBride 2001; McBride et al. 2003; Chang et al. 2004); and the combined influence of multi-scale interactions (Chang et al. 2005a, b; Tangang et al. 2008; Qian et al. 2013; Chen et al. 2015b). On the other hand, the SCS-MC deep convection is known to have strong influence on higher latitude Rossby waves through the wave train emanated from the SCS-MC and western Pacific warm pool region (see the review in Stan et al. 2017). Due to the complex land-sea distribution and topography, and the complicated multi-scale influential factors, current state-of-the-art global climate models and numerical weather prediction models cannot reproduce many observed features of precipitation over the MC (Kim et al. 2018). Therefore, understanding the climatology and variability of precipitation over the SCS-MC region is of great

* *Corresponding author*
  E-mail: mongminglu@ntu.edu.tw

importance to improve weather and climate forecast in the local area and over the world.

Taiwan joined the international effort by conducting the South China Sea Two-Island Monsoon Experiment (SCSTIMX) in corporation with the international project "Years of the Maritime Continent (YMC)" (http://www.jamstec.go.jp/ymc/docs/YMC_SciencePlan_v2.pdf) to study convective and large-scale dynamic processes over the SCS-MC region. The period 2017 - 2019 was designed as an extended observation period (EOP) with two wintertime intensive observation periods (IOPs) in December of 2016 and 2017 at Taiping Island and Dongsha Island. Intensive field observation at two islands aimed at understanding convective process, diurnal cycle and the interaction of convective and dynamical processes such as extratropical-tropical interactions, intraseasonal oscillations (ISO), or ISO-tropical cyclone (TC) interactions in this region (Chen et al. 2020; Kuo et al. 2020; Lu et al. 2020; Sui et al. 2020). This study is part of the SCSTIMX endeavour specifically focus on documenting the modulation effects of MJO and CCEWs on the subseasonal peak precipitation event over the SCS-MC region. The motivation is to provide useful observational evidence that can be used to evaluate weather and climate forecast models and improve the prediction on sub-seasonal to seasonal time range (abbreviated as S2S).

S2S prediction aims at forecasts from about 2 weeks to a season ahead. The forecast period shows the lowest prediction skill compared with the shorter-term forecasts for weather and longer-term forecasts for seasonal or interannual climate variability, because the S2S time range is too long for the memory of the atmosphere to influence and too short for the boundary forcing such as SST anomalies to be felt. The most important sources of the S2S predictability are: the MJO, soil moisture, snow cover, stratosphere-troposphere interaction, and ocean conditions (Vitart and Robertson 2019). Understanding how MJO and CCEWs modulate the major precipitation peaks will help us preparing for further research on the multiple scale interactions and influence on the precipitation in the SCS-MC region and improving S2S prediction.

The variability of tropical precipitation due to MJO and CCEWs is a subject that has been fervently studied. For example, Lubis and Jacobi (2015) applied frequency-wavenumber analysis on precipitation data to extract the variance of each type of the four prominent waves. In the present study we have a different purpose from the previous studies. We will focus on the subseasonal peak precipitation event over the SCS-MC region to assess how MJO and CCEWs make temporal and intensity influence on the peak event. The temporal influence is identified as the proportion of the time of the peak event during with convective phases of the waves. The intensity influence is measured by the ratio of mean rainfall intensity during the convective phase in contrast to the suppressed phase. The MJO and CCEWs

are identified based on OLR data. Given the planetary-scale structures of MJO and CCEWs, it is reasonable to identify the waves based on OLR instead of precipitation because the later can be influenced by more local factors such as the land and sea contrast, orographic, and meso-scale effects (Moron et al. 2010). OLR variability reflects the coherent large-scale dynamic and convective patterns (Kiladis et al. 2014). It is a good proxy of tropical deep convection. We invented the term of the subseasonal peak precipitation event for the objective of using it as a target that can be evaluated in S2S prediction models (Vitart and Robertson 2019). We hope to make our findings relevant to the end users, for whom it is more useful to know the precipitation predictability at the interested specific locations rather than an overall estimation of the CCEWs.

This paper is organized as follows. Section 2 introduces the data and the detection methodology of MJO and CCEWs, convective and suppressed phases, and the subseasonal peak precipitation event. Section 3 presents the precipitation climatology and the sub-seasonal peak precipitation defined in this study and its importance. In section 4, we will discuss how MJO and CCEWs modulate the peak precipitation from the multi-year climatological perspective. In section 5, we use the SCSTIMX years to illustrate the MJO and CCEWs modulation in individual winters and discuss the contrast in these two years. Section 6 is a summary of findings and concluding remarks.

2. DATA AND METHODOLOGY

2.1 Data Source

In this study, the precipitation data is mainly based on CMORPH (CPC MORPHing technique) V1.0 data from 1998 to 2018 obtained from ftp://ftp.cpc.ncep.noaa.gov/precip/CMORPH_V1.0/. The integration algorithm is fixed and the input level 2 passive microwave retrievals of instantaneous precipitation rates are from identical versions throughout the entire data period. It includes the raw, satellite only precipitation estimates, corrected, and gauge-satellite blended precipitation products. Additionally, TRMM/GPM era from January 1998 to the present was processed to extend the data range (Joyce et al. 2004; Xie et al. 2017). The deep convection location is based on the interpolated daily outgoing longwave radiation (OLR) version 1.2 (Lee 2011) from National Oceanic and Atmospheric Administration (NOAA) Climate Data Record (CDR), which can be downloaded from the website of NCEI (National Centers for Environmental Information), NOAA (https://www.ncei.noaa.gov/data/outgoing-longwave-radiation-daily/access/). Large-scale circulation analysis is based on the ERA-Interim (Berrisford et al. 2011), with horizontal resolution 0.75° × 0.75°, from the European Centre for Medium-Range Weather Forecasts (ECMWF) and made available from the website of the ECMWF (https://www.ecmwf.int/en/

forecasts/datasets/archive-datasets/reanalysis-datasets/era-interim).

2.2 MJO and CCEWs Identification

We follow Wheeler and Kiladis (1999) to identify MJO and CCEWs. The first step is to remove the seasonal cycle by subtracting from each grid point the long-term mean and the first three harmonics of each year based on the 1979 - 2018 period. Note that different from the procedure in Wheeler and Hendon (2004) we did not remove the ENSO interannual variability. To retain the full signal of the waves (Kiladis et al. 2009), the anomalies of symmetric and anti-symmetric components of the waves are not decomposed. Then, the Fourier transform in longitude is performed, followed by another transform in time. Fourier coefficients outside the range of the filter are then set to zero and the filtered data are obtained by performing the inverse transform. The spectral bands used in space-time filter technique for CCEWs are based on the dispersion relation Eq. (1) derived by Matsuno (1966).

$$\omega^2 - k^2 - \frac{k}{\omega} = 2m + 1, \quad m = 1, 2, ... \quad (1)$$

where k is the wavenumber, ω is the frequency of the waves, and m is the meridional mode index of the wave which is considered in the equivalent depth in the program. The wavenumber, frequency bands, and equivalent depths for each tropical mode are presented in Table 1. Note that the wavenumber of eastward waves such as Kelvin wave and MJO is positive and the westward ones such as ER wave and MRG waves/TD-type disturbance (MT waves) is negative. The power spectrum of Kelvin waves, ER waves, MT waves, and MJO with OLR data from 1981 to 2018 applied are found in Fig. 1. The first three waves follow the dispersion curves described by Eq. (1), whereas for MJO there is no suitable dispersion curves to fit. This calculation is provided by Carl Schreck, III (SUNY at Albany, see https://ncics.org/portfolio/monitor/mjo/) and the function can be applied to NCAR Command Language (NCL) pro-

grams (see https://www.ncl.ucar.edu/Document/Functions/User_contributed/kf_filter.shtml).

2.3 Convective and Suppressed Phases Identification

The modulation of MJO and CCEWs on precipitation has been studied by many scientists (Roundy and Frank 2004; Tulich and Kiladis 2012; Yasunaga and Mapes 2012; Lubis and Jacobi 2015). For instance, Lubis and Jacobi (2015) analyzed Tropical Rainfall Measuring Mission (TRMM) daily data and found that variability of tropical precipitation due to CCEWs behaves relatively variously over different seasons and locations and, on average, the integrated contribution reached 16 - 20% of the intraseasonal (2.5 - 72 days) precipitation variance in the tropics. Van der Linden et al. (2016) analyzed the daily rainfall based on an extensive station database and the gridded Asian Precipitation-Highly Resolved Observational Data Integration Toward Evaluation of Water Resources (APHRODITE) product (Yatagai et al. 2012) over southern Vietnam during the rainy season (May to October). They found that the frequency of occurrence of intense daily rainfall larger than 25 mm was significantly enhanced during wet phases, whereas the magnitude of rainfall anomalies was related to the wave's amplitude only in the MJO and ER cases. In addition to the contribution of each wave to the precipitation, they also found that the waves can modulate tropospheric moisture convergence over the region. The influence on the depth of the monsoon flow and the vertical wind shear is also important for MJO. Schlueter et al. (2019) analyzed the CCEWs modulation on northern Africa using TRMM and the Climate Hazards Group Infra-Red Precipitation with Station (CHIRPS) V.2 dataset (Funk et al. 2015) and found that the modulation varies from less than 2 to above 7 mm d^{-1} depending on the wave type. Based on the aforementioned studies and the references therein, in this study we use the rank order of the wave-filtered OLR to flag the dates of the study period (1998 - 2015) as a day of the "convective", "no signal", and "suppressed" phases of MJO and individual CCEWs. The convective status of each wave is determined according to the threshold values of the wave-filtered OLR. The threshold values are defined

Table 1. The range of planetary zonal wavenumber, period (days) and equivalent depth (m) chosen for filtering MJO, CCEWs, and corresponding thresholds to distinguish convectively active and suppressed phase (filtered OLR, W m^{-2}). "N/A" means the region of filtering does not follow the dispersion curve. The wavenumber-frequency ranges for MJO, Kelvin wave, ER wave are based on Wheeler and Kiladis (1999), and MT wave is based on Frank and Roundy (2006).

Tropical modes	Planetary zonal wave-number	Period	Equivalent depth	Wave activity thresholds for filtered OLR	
				Convectively active	Suppressed
MJO	1 to 5	30 to 96	N/A	-8.84	8.69
Kelvin wave	1 to 14	9.7 to 48	8 to 90	-7.44	7.37
Equatorial Rossby wave	-10 to -1	2.5 to 30	8 to 90	-7.48	7.33
MRG wave/TD-type disturbunce	-14 to 0	2.5 to 10	N/A	-7.97	7.95

Fig. 1. The wavenumber (k)-frequency (ω) spectra of OLR data from 1981 to 2018 between 15°S and 15°N, without symmetric partition. The thick polygons indicate domains for the filtered MJO, Kelvin waves, ER waves, and MRG waves/TD-type disturbances.

3. CLIMATOLOGICAL FEATURES OF THE PRECIPITATION

3.1 Evolution of the Tropical Precipitation Density During the Boreal Winter

The precipitation over the land bridge between Asia and Australia is characterized by its clear seasonal migration during the boreal winter months. In order to see the geographical features of the movement of the major precipitation centers, we plot the climatological monthly precipitation density calculated as the ratio of the precipitation at each grid point with respective to the total precipitation summed over the entire tropical belt between 20°N and 20°S in Fig. 2. The major precipitation areas highlighted in Fig. 2 are the areas with higher proportion of the contribution to the total precipitation over the entire tropical belt. If we focus on the land bridge between Asia and Australia and the marginal seas, we can see the high precipitation density area moves from the eastern equatorial Indian Ocean eastward to South Pacific Convergence Zone (SPCZ) during the period from November to February. In November the areas of high precipitation density appear over the eastern equatorial Indian Ocean, southwest Borneo, and Papua New Guinea. In December, the precipitation center over eastern equatorial Indian Ocean becomes more concentrated alone the equator and extended eastward to the Java Sea and South China Sea. It is evident in Fig. 2b that the SCS-MC region is the most prominent precipitation region. Another outstanding region is the Intertropical Convergence Zone (ITCZ) over the tropical Pacific. The main precipitation region shifts eastward from the SCS to South Pacific during the four months from November to February. In March and April, in contrast to the high precipitation density in the Amazon Basin, the SCS-MC region is relatively dry. The precipitation density over SPCZ is also weakened, as a contrast to the enhanced precipitation density from February to April over the western Pacific warm pool region (0 - 10°N, 150 - 170°E). Over north Australia and the marginal seas between Australia and Indonesian islands, such as the eastern Indian Ocean, the Timor Sea, the Arafura Sea, and the Carol Sea, the months with the highest precipitation density appear in January to March.

The temporal and spatial characteristics of the precipitation seasonal cycle associated with the low-level monsoonal flow over the land bridge between Asia and Australia and the marginal seas are illustrated in the 20-year (1998 - 2017) climatology based on the ERA-Interim wind data and CMORPH precipitation (Fig. 3). The cyclonic flow formed by the northeasterly winds associated with the East Asian winter monsoon deflected by weakened Coriolis force when it flows southward, with the confluence of southerlies from Southern Hemisphere can be seen during the winter half year. However, with winter monsoon becoming weaker in March and April, the precipitation weakens as well in these two months. The topographic effect on winter monsoon (Chang
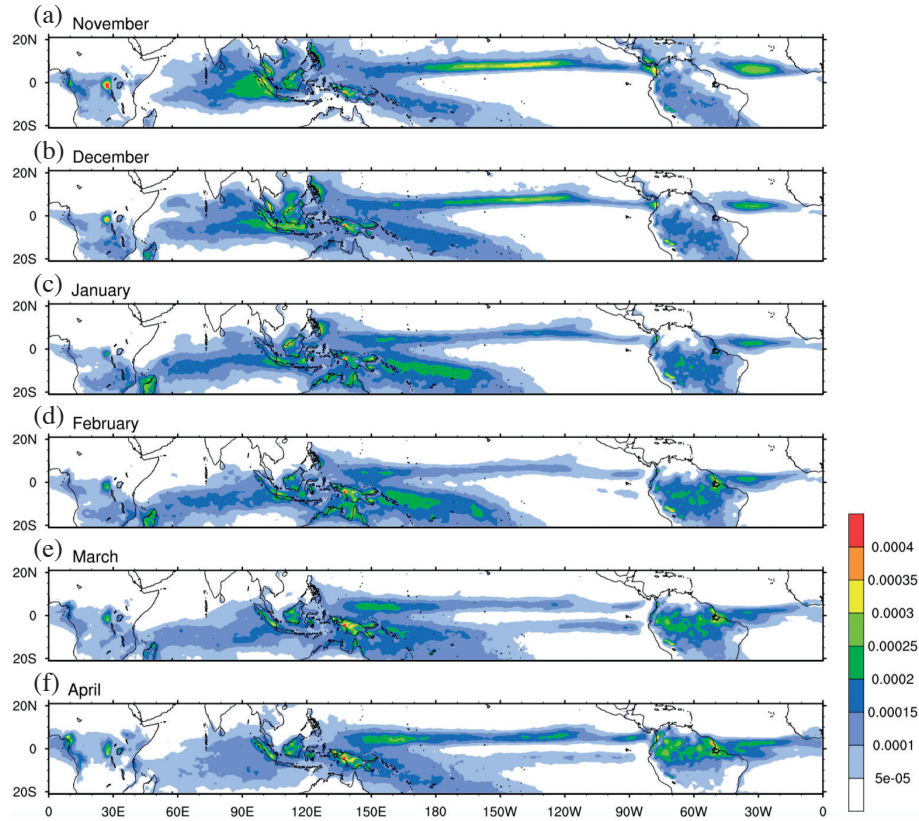
by the first (q_{25}) and third (q_{75}) quartiles of the filtered daily OLR anomalies collected during the boreal winter half year (November to April) from 1998 to 2015 of all grid points in the SCS-MC region bounded by the longitudes of 105 and 135°E and latitudes of 15°S and 15°N. When the filtered OLR anomaly is lower than q_{25} the day is categorized to the convective phase, while if it is higher than q_{75} the day is categorized to the suppressed phase, otherwise the day is categorized as no signal. The thresholds for each type of waves are summarized in Table 1.

2.4 Sub-Seasonal Peak Precipitation Identification

This study aims to provide useful observational evidence to support S2S prediction. A new term "sub-seasonal peak precipitation event" (for brevity, it is also called "peak precipitation" in this paper) is introduced as a focus of the analysis. The peak precipitation is defined as a period of successive three pentads during which the accumulated rainfall amount reaches the maximum compared with all cases of the running 15-day (3-pentad) accumulated rainfall within November to February. Note that the four months of November to February is the wettest four months during the entire boreal winter half year for SCS-MC characterized by the precipitation annual cycle in this region. A focus of this study is to investigate how MJO and CCEWs modulate the interannual variability of the occurrence time and mean precipitation intensity of the peak precipitation.

Fig. 2. The climatological monthly precipitation density calculated as the ratio of the precipitation at each grid point with respective to the sum over the entire tropical belt (20°S - 20°N) in (a) November, (b) December, (c) January, (d) February, (e) March, and (f) April. The data is CMORPH v1.0, 1998 - 2018.
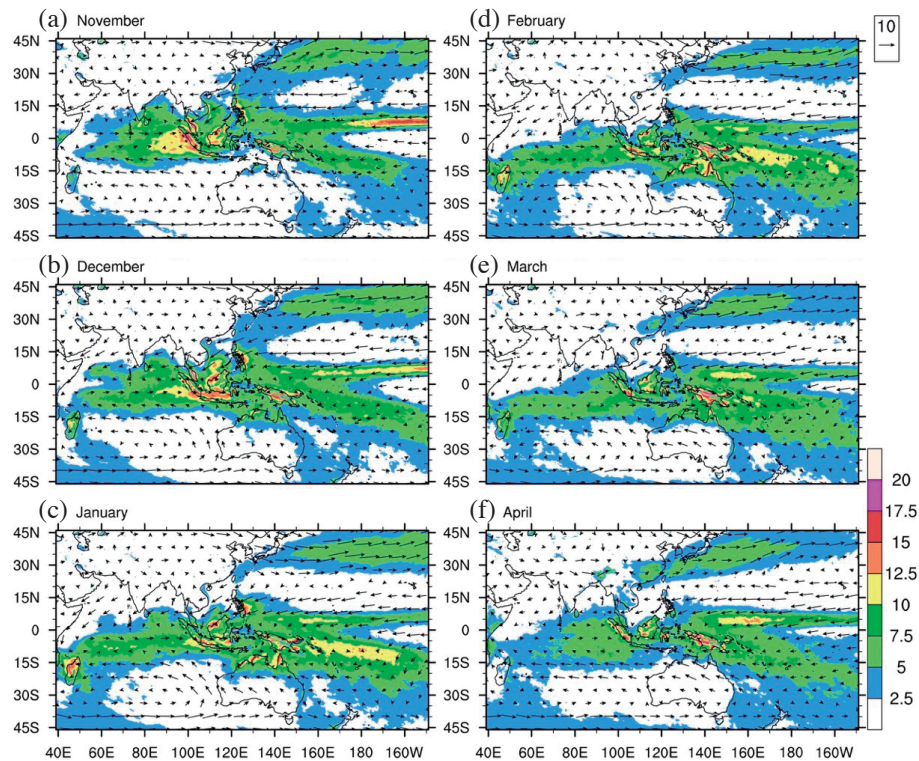

Fig. 3. Climatological (1998 - 2018) monthly mean CMORPH precipitation (shaded, mm day^{-1}) and ERA-Interim 850-hPa wind (vectors, m s^{-1}) in (a) November, (b) December, (c) January, (d) February, (e) March, and (f) April.

et al. 2005a, b) that leads to the enhanced precipitation over eastern coast of Philippine, Vietnam, Malay Peninsula, and western Sumatra can be identified in Figs. 3a and b. Also note that the most intense rainfall over SCS occurs in December, which is associated with Borneo vortex, occurring as the monsoon meets the equatorial westerlies over western MC so that the distribution of wind field leads to a quasi-stationary low-level cyclonic circulation over northwest Borneo (Johnson and Houze 1987). Associated with the onset of Australian monsoon (Hung and Yanai 2004) the westerly component of the low-level winds over the equatorial eastern Indian Ocean becomes intensified from December to January which pushes the inter-hemisphere confluence zone from eastern Indian Ocean to the western South Pacific.

3.2 SCS-MC Sub-Seasonal Peak Precipitation in Boreal Winter

As mentioned in section 2.4 this study aims to document how waves modulate the timing and precipitation intensity of the peak precipitation in the SCS-MC region, where the total precipitation amount during the boreal winter half year on average account for about 40 - 70% of the annual total rainfall. Due to the complicated geographical inhomogeneity of the precipitation distribution, we separate the SCS-MC region to box areas indicated in Fig. 4. Box-a covers Taiwan, the Luzon Strait, and the northeastern SCS. Box-b and Box-c cover the central SCS, Box-d covers the east coast of the Philippines and the western Philippine Sea, and Box-e covers the southern SCS and western Borneo. Dongsha Island is located in Box-a and Taiping Island is in Box-b. Both Box-d and Box-e include the areas with very high percentage (> 40%) of the annual total precipitation in boreal winter, especially the eastern Philippine, Sumatra, and Borneo. Winter precipitation plays a significant role in annual rainfall over SCS-MC region.

Figure 5 shows the annual cycle of the precipitation pentad climatology (1998 - 2018) in five box areas. Box-a shows two peaks of which the first peak occurs around the 32nd Pentad (5 - 9 June) and the second peak occurs around the 43rd to 48th (1 - 28 August) corresponding to the peaks of Mei-Yu and typhoons in Taiwan and surrounding area. Box-b and Box-c show weaker Mei-Yu peak compared with Box-a, but a long tail lasting until late December after the typhoon peak. Box-d shows in addition to the peaks in summer there is a precipitation peak in January. Box-e shows minimum precipitation during the typhoon season but maximum precipitation in late December and early January. Consistent with what we saw in Fig. 2 that for the box areas of a - d the major wet period during the winter half year is November to February. The SCS-MC region becomes relatively dry after February because the tropical precipitation center shifted from the Indian Ocean and MC to the SPCZ and the Amazon Basin. The favorable month for the peak precipitation can

be clearly seen in the monthly fraction of the winter precipitation totals (Fig. 6). Figure 6 shows that over the SCS the peak precipitation occurred in November and December, while the January precipitation over the western Philippine Sea, the Celebes Sea, the Sulu Sea and the eastern SCS in general accounts for about 20% of the winter totals.

Figure 7 shows the mean occurrence time of the mid-pentad of sub-seasonal peak precipitation event (see section 2.4 for definition) and its standard deviation. The southwest-northeast oriented belt region extended from Sumatra through central SCS to the western North Pacific to the east of Taiwan, mainly corresponding to the box areas of a - c, shows the peak precipitation in Vietnam occurs in November, which is earlier than the rest areas of the region. The standard deviation of the occurrence time over eastern coast of Vietnam and the SCS is very small. It suggests that over this area we should expect a drying tendency since January. On the other hand, the standard deviation of the peak precipitation occurrence time in Box-d and Box-e is relatively large and lags Box-b for about one month. It is consistent with Fig. 5 that the peak precipitation in Box-d and Box-e occurs in late December and early January, respectively.

The importance of predicting the peak precipitation occurrence time and intensity accurately can be understood when seeing the percentage of the 15-day accumulated rainfall amount relative to the four-month totals of November to February (Fig. 8). For Box-b and Box-c the percentage is larger than 50%. The significance of the peak precipitation is outstanding over northeastern SCS, in particular, to the west of Luzon island.

4. MJO AND CCEWS' MODULATION ON SCS-MC PRECIPITATION

To assess how much the MJO and CCEWs can modulate the precipitation in SCS-MC region, we calculate the average difference of the precipitation rate between the "convective" and "suppressed" phases by dividing the sums of precipitation totals during the "convective" and "suppressed" phases by the total days of these two phases, respectively. The 850-hPa wind anomalies are also processed following the same rules. The phase identification procedure is described in section 2.3. Precipitation and wind are re-gridded to the same grid format as the OLR data for analysis convenience. The investigation period is four months from November to February. Days with more than one type of waves are excluded. It should be noted that the days with more than one type of waves mostly (> 50%) observed over the belt of 5 - 15°N. results shown in Figs. 9a - d suggest that the composite precipitation patterns in both the suppressed and convective phases for all MJO and CCEWs bear a similarity in their geographic characteristics. The geographic similarity between different waves in both convective and suppressed phases suggests that the wave enhancement is

strongly modulated by the climatological preference. In other words, the modulation is strong in the places with more seasonal rainfall (Fig. 3). However, in the convective and suppressed difference diagrams (Fig. 9, left column), where the precipitation amplitude is represented in terms of the times of the standard deviation of the monthly precipitation in 20 years (1998 - 2017) and the wind vectors are the difference of the 850-hPa wind anomalies between convective and suppressed phases, a striking land and ocean contrast emerges in the diagrams of MJO and ER waves. The difference over the Philippine Sea and western Pacific is in general larger than that over the land areas. Over the Indonesia islands, Borneo, and New Guinea, we see negative contribution of the active phases of MJO and ER (Figs. 9a, c).

The precipitation rate in convective days is particularly large over eastern coast of Philippine and northwestern Borneo with the strongest modulation effect by the MT waves. Over northwest Borneo the Kelvin and MT wave modulation is stronger than other two types of CCEW. However, the wind contrast between the convective and suppressed phases in the deep tropics south of 15°N is small in the MT wave modulation (Fig. 9d-3) compared with other types. The ER wave modulation (Fig. 9c-3) suggests an enhancement of the low-level convergence outside of the deep tropics, north of 15°N, that weakens the northerly monsoonal flow over the SCS. The Kelvin wave modulation (Fig. 9b-3) shows strongest effect on the anomalous cyclonic circulation over the southern part of the SCS. Similar anomalous
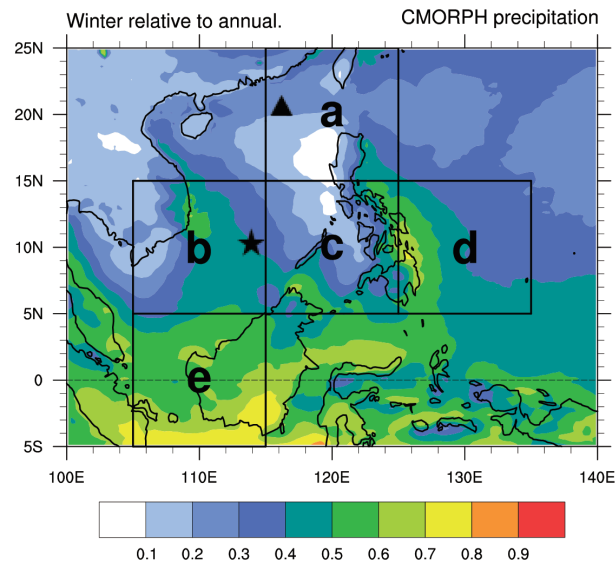

Fig. 4. The proportion of boreal winter half-year (NDJFMA) rainfall amount to the annual totals. Five boxes a - e are defined as the focus for this study: Box-a covers Taiwan, the Luzon Strait, and the northeastern SCS. Box-b and Box-c cover the central SCS, Box-d covers the east coast and the western Philippine Sea, and Box-e covers the southern SCS and western Borneo. Dongsha Island (triangle) is located in Box-a and Taiping Island (star) is located in Box-b.
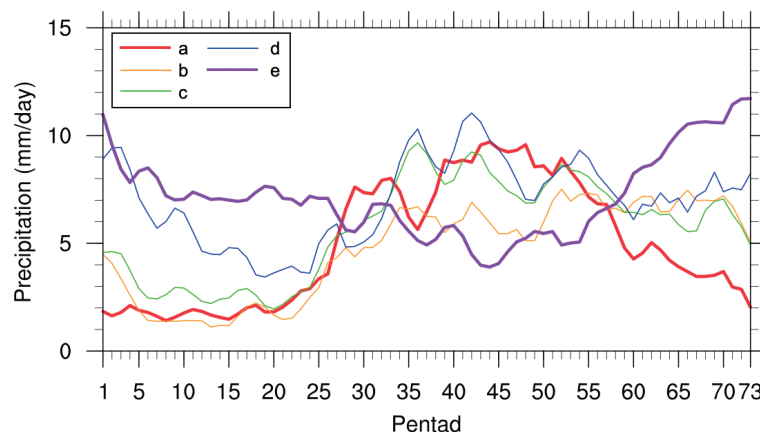

Fig. 5. The annual cycle of climatological (1998 - 2018) precipitation in pentads (unit: mm day^{-1}), smoothed by three-pentad running mean, for the five boxes areas in Fig. 4, Box-a (red), Box-b (orange), Box-c (green), Box-d (blue), Box-e (purple).
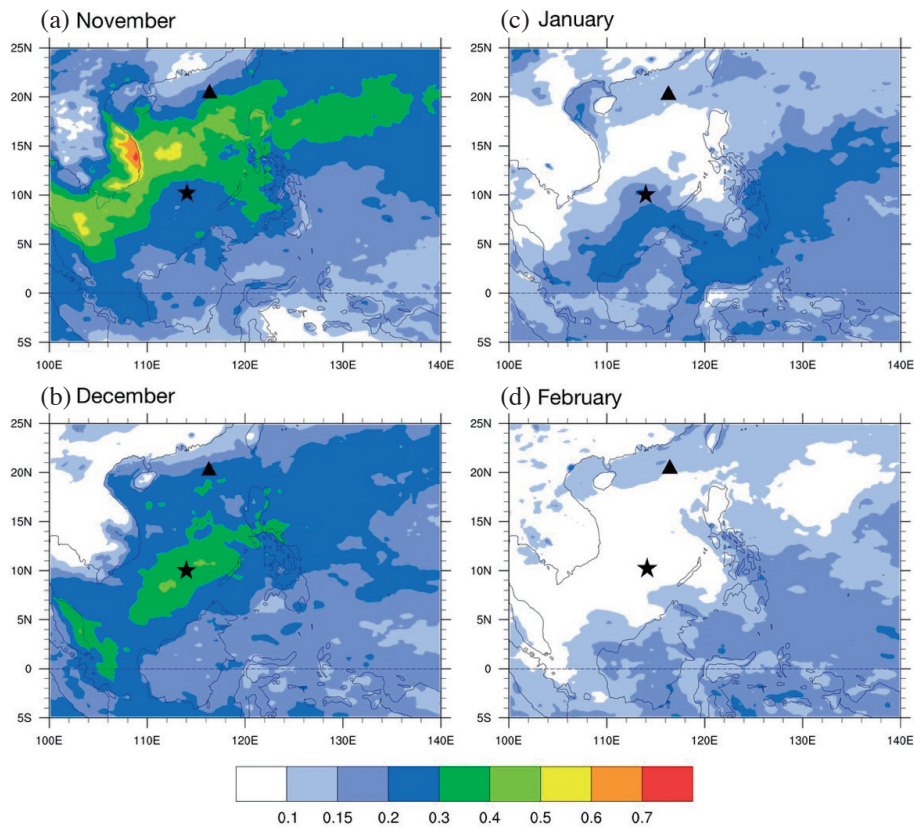
Fig. 6. The proportion of the monthly rainfall amount in (a) November, (b) December, (c) January, (d) February to the winter half-year (NDJFMA) totals. Dongsha (triangle) is located in Box-a and Taiping Island (star) is located in Box-b. Dongsha (triangle) and the star marks are the locations of Dongsha and Taiping islands respectively where the SCSTIMX experiments launched.
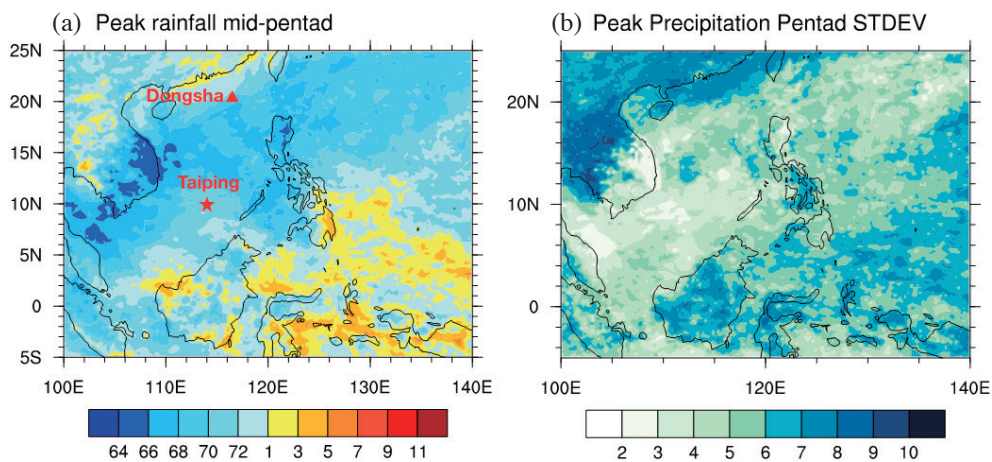

Fig. 7. (a) Climatological (1998 - 2017) mean occurrence time of the mid-pentad of sub-seasonal peak precipitation event and (b) its standard deviation (unit: pentad). The triangle and the star marks are the locations of Dongsha and Taiping islands respectively where the SCSTIMX experiments launched.
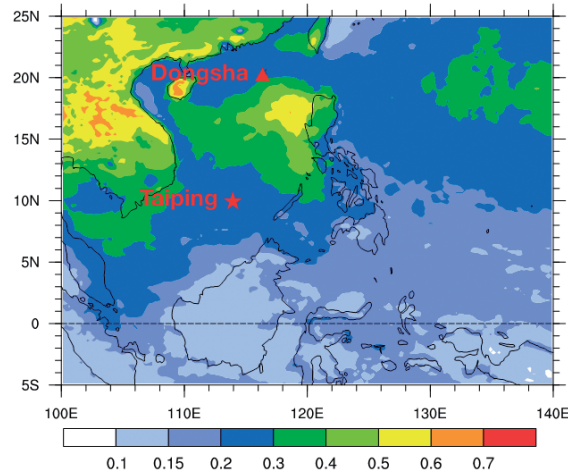
Fig. 8. Cumulative rainfall amount during sub-seasonal peak precipitation event relative to November to February four-month totals. The triangle and the star marks are the locations of Dongsha and Taiping islands respectively where the SCSTIMX experiments lunched.
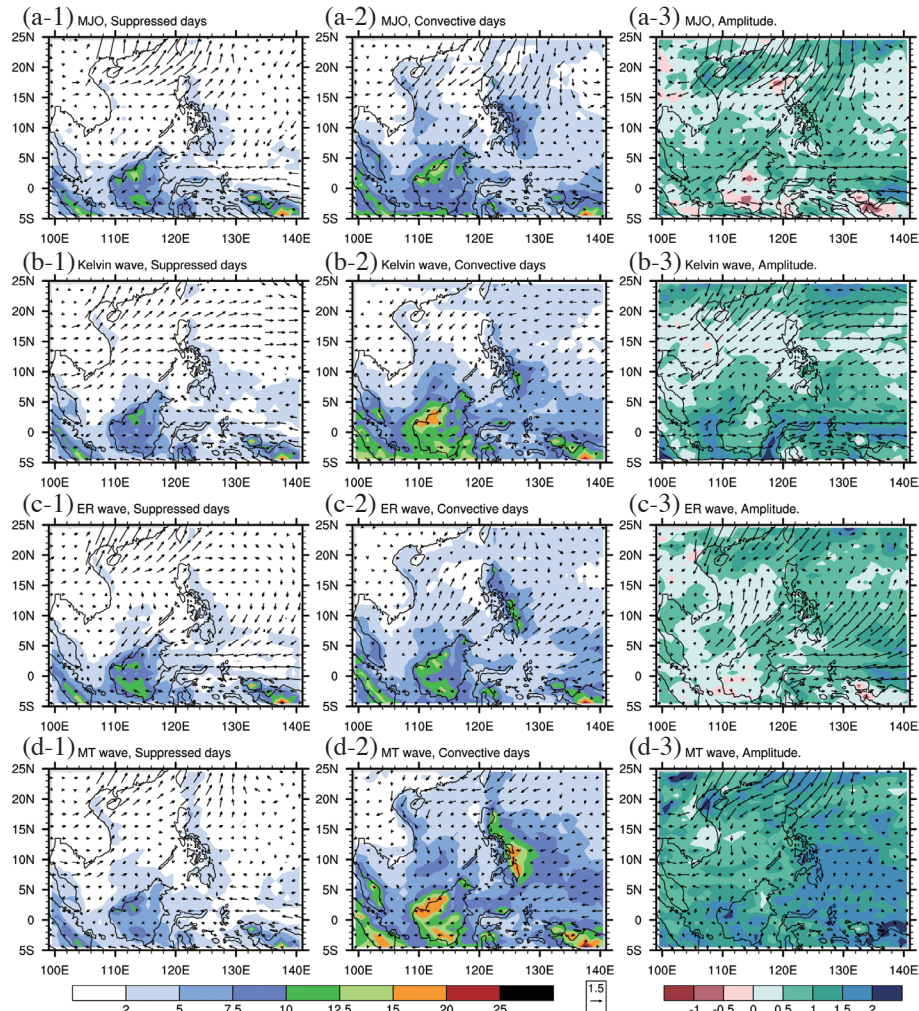

Fig. 9. Mean precipitation rate (unit: mm day^{-1}) and anomalous 850-hPa wind (unit: m s^{-1}) for (a) MJO, (b) Kelvin waves, (c) ER waves, (d) MRG waves/TD-type disturbance in suppressed and convective phases and their difference. Left column (a-1) to (d-1): daily averaged precipitation and composited 850-hPa wind anomaly for suppressed phase of the waves (days were chosen according to filtered OLR at each grid); middle column (a-2) to (d-2): for convective phase; right column (a-3) to (d-3): the precipitation amplitude in each grid expressed as times of the standard deviation computed using the monthly precipitation of ND(-1)JF(0), 1999 - 2018, and mean difference of 850-hPa wind anomalies between convective and suppressed phases of the waves.

cyclonic circulation can be identified also in the MJO modulation diagram (Fig. 9a-3) but the center is located near central Philippines at 13°N and 119°E. The MJO modulation shows stronger influence on the equatorward low-level winds in particular over the western rim of the Pacific and the Philippine Sea. The low-level westerlies over the equatorial region (5°S - 5°N) is enhanced during the MJO convective phase. The result suggests that a substantial portion of the days identified as the convective phase of the MJO over the SCS-MC region belong to Phases 5 and 6 of the MJO (see Fig. 6 in Woolnough 2019) identified using the RMM index (Wheeler and Hendon 2004). In summary, we interpret the result as CCEWs have small influence on the variability of daily rainfall totals in SCS-MC region. Precipitation rate along eastern coast of Philippine, Borneo, Sumatra, and New Guinea remains larger than other location in the region, regardless of the wave type. The wave enhancement is more clear in the places with abundant seasonal rainfall where the rainfall is strongly influenced by wind-terrain interaction as discussed, for example, in Chang et al. (2005b).

After seeing the overall modulation of MJO and CCEWs, we will evaluate the relationship with the sub-seasonal peak precipitation event (section 2.4). We checked how the waves modulated the occurrence time of the peak precipitation but did not find significant influence (figures not shown). Then we checked the proportion of the days with convective phase of the waves during the peak events, in contrast to the days not counted as convective, and named the proportion as the temporal modulation of the waves. Since the total number of days of the sub-seasonal peak precipitation event is fixed as 15 days, the temporal modulation can be measured by the count of days where MJO or CCEWs are in convective phase (Fig. 10). Figure 10a shows that over the ocean more than 30% of the days of the peak precipitation belongs to the convective phase of MJO. ER (Fig. 10c) shows similar number of convective days as the MJO, while MRG/TD (Fig. 10d) and Kelvin waves (Fig. 10b) show relatively less days of convective phases. Both ER and MRG/TD influence shows a clear contrast pattern between the equator and off-equator belts, while the Kelvin shows a maximum zonal pattern near the equator. The contrast between different waves is consistent with their dynamic structure in theory (Matsuno 1966) and observation (Kiladis et al. 2009). The sharp contrast between ocean and land areas of MJO influence (Fig. 10a) is striking. MJO shows large modulation on the peak precipitation over ocean than over land.

Next, we assess the MJO and CCEW modulation on rainfall intensity by computing the relative mean precipitation intensity in the days of convective phases versus the days of non-convective phases of the waves (Fig. 11). We see clear contrast between MJO and other waves. Figures 11b - d show clear enhancement of mean precipitation intensity at the convective phases of the CCEWs during the peak precipitation event, while Fig. 11a shows almost no enhancement at the convective phases of the MJO. The result suggests that peak rainfall events tend to occur when the MJO's convective phase is not over the SCS-MC. It seems imply that MJO modulation is less effective than the local modulation on rainfall intensity. This subject is currently under investigation and the result will be published in a separate paper.

5. CASE STUDIES OF THE SCSTIMX WINTERS

In this section we will demonstrate how the analysis can be applied to monitor the MJO and CCEWs modulation on the SCS-MC precipitation by showing the cases of two SCSTIMX winters, namely, the 2016/17 and 2017/18 winters. We first compared the annual cycle and the timing and intensity of the sub-seasonal peak precipitation events during the SCSTIMX winters with the 20-year climatology over the five box areas (Fig. 12). On average the blue (2016/17) and red (2017/18) lines are above the dark-grey (20-year mean) line, which means that these two years are wetter than the climatology. This is consistent with what one expects for the precipitation anomalies over SCS-MC region during a La Niña phase. According to the Niño indices published at the website of NOAA/Climate Prediction Center (https://origin.cpc.ncep.noaa.gov/products/analysis_monitoring/ensostuff/ONI_v5.php) the periods of JAS 2016-NDJ 2017 and SON 2017-FMA 2018 are the ENSO cold episode based on the value of Niño3.4 index. However, we notice that the wet anomaly is less clear in Box-e. Also, the precipitation fluctuation in Box-e (Fig. 12e) has higher frequency than other sub-areas. This is consistent with the earlier discussion (Fig. 9) that over the equatorial Indonesia islands the active phases of MJO and ER do not enhance precipitation over the islands.

The focus period of the present study, which is from Pentad 62 (2 - 6 November) to Pentad 13 (25 February to 1 March), is marked by the light-grey box in Fig. 12. It is evident that a large portion of the seasonal precipitation is contributed by few large episodes. The peak events at each box area are marked by the filled circles with dotted lines attached. Here the filled circles indicate the medians and the dotted lines the inter-quartile range of the occurrence time of the peak events determined at each grid point of the 0.25° × 0.25° of the longitude and latitude grids within the sub-areas of Boxes a - e. The distance between the median pentads of the peak events in two winters and climatology are closest in Box-b and Box-c, where the three medians are located within three pentads (Pentad 67 - 70, 27 November to 16 December). The interannual difference is largest at Box-d where 2017/18 is earlier than normal and 2016/17 is slightly later than normal. The distance between the 2016/17 and 2017/18 medians is seven pentads. The inter-grid difference
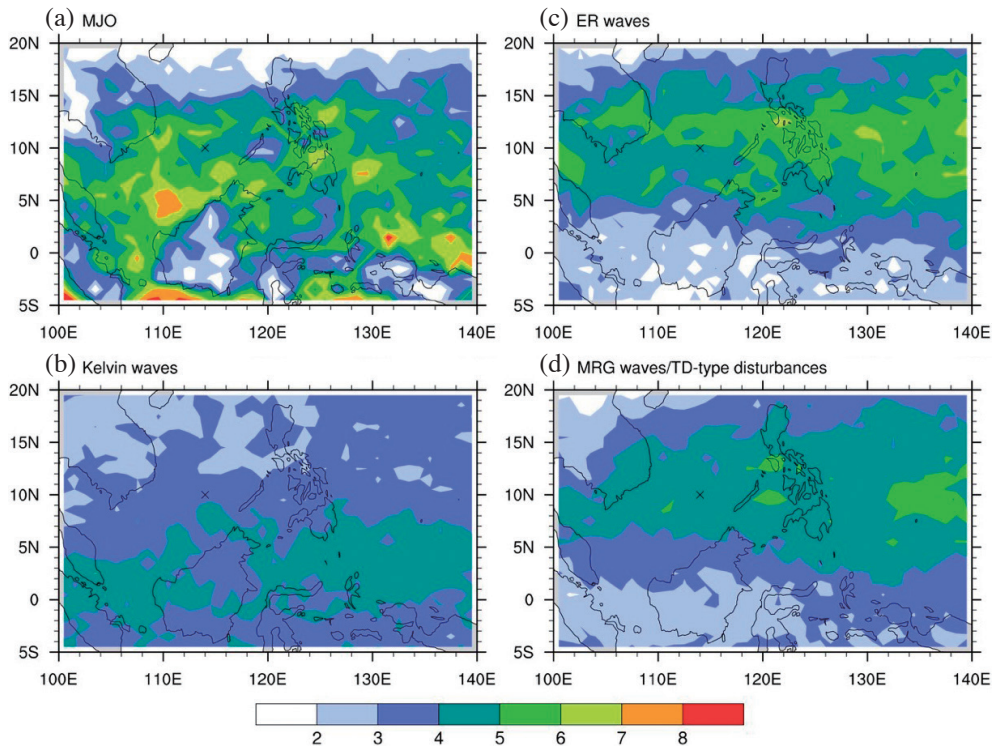
Fig. 10. Averaged number of days with convective phase of (a) MJO, (b) Kelvin wave, (c) ER wave, and (d) MRG/TD-type disturbance during the 15-day sub-seasonal peak precipitation event from 1999 to 2018. Days with more than one type of waves are excluded.
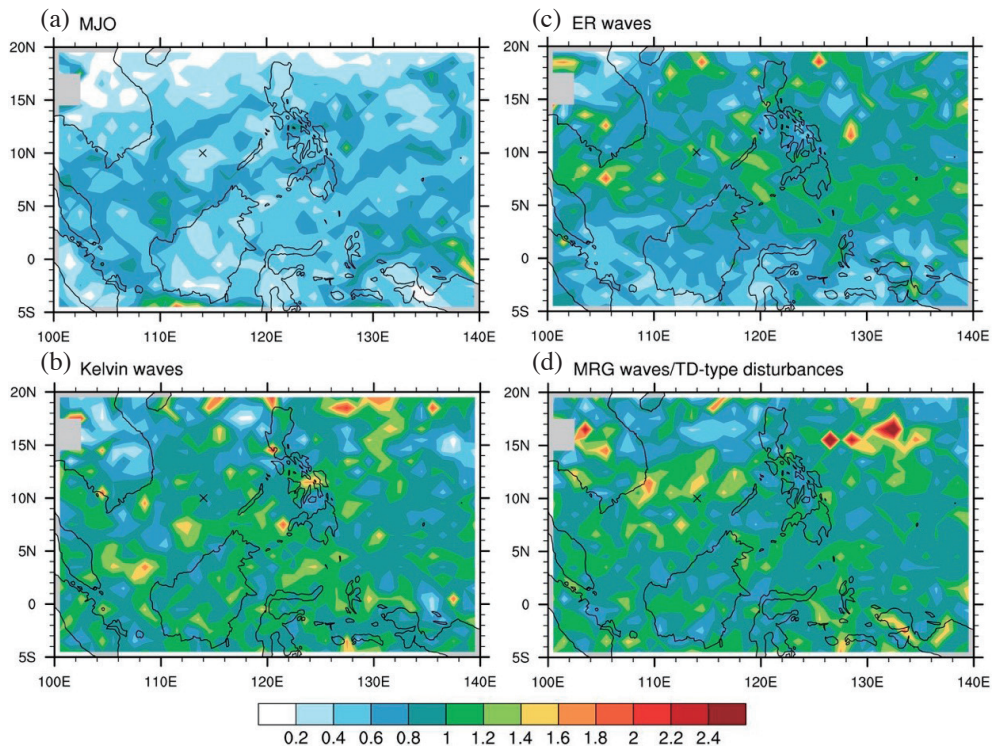

Fig. 11. The relative rainfall intensity averaged over the days categorized to the convective phases and the days not categorized to the convective phases of (a) MJO, (b) Kelvin wave, (c) ER wave, (d) MRG/TD-type disturbance. The data is from 1999 to 2018. Days with more than one type of waves are excluded.
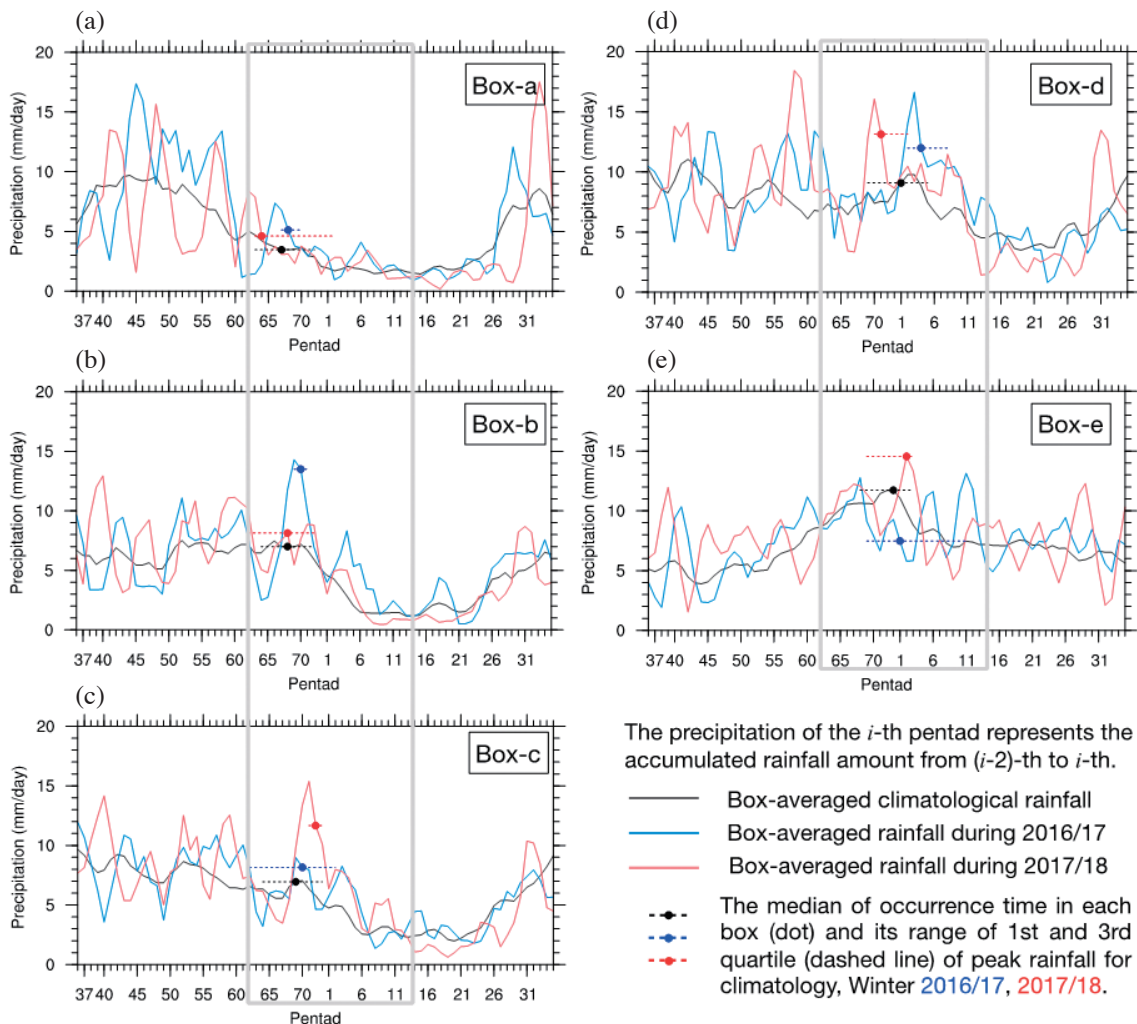
Fig. 12. Climatological (1998 - 2017, dark-grey), 2016/17 (blue), and 2017/18 (red) precipitation (unit: mm day^{-1}) annual cycle in 3-pentad running mean for the Box-a to Box-e defined in Fig. 4. The boreal winter period of this study (NDJF) is marked by the light-grey boxes. The occurrence time of the sub-seasonal peak rainfall event is identified at each grid point. The median determined by the occurrence time of all grid points within a Box is marked by the filled circle attached with the dotted line showing the inter-quartile range.

within the Box area, represented by the inter-quartile range, is largest in Box-e during the 2016/17 winter. Due to the large inter-grid difference, the 2016/17 sub-area mean rainfall peak in Box-e occurred much later than the climatology. Nevertheless, it is evident that the peak event is indeed the most important sub-seasonal rainfall episode during the boreal winter season. For Box-a to Box-c (Figs. 12a - c), the timings of the peak events in the two winters are very close to the climatological mean, while Box-d and Box-e (Figs. 12d - e) reveals larger variance. The phenomenon is consistent with standard deviation of the occurrence of peak rainfall events in climatological analysis illustrated in Fig. 7. Figure 12 implies that the peak rainfall occurrence time in winters 2016/17 and 2017/18 over Box-b and Box-c are locked to the seasonal cycle with enhancement in amplitude by the modulation of the subseaonal peak event. For Box-b the 2016/17 peak is more intense than the 2017/18

(Fig. 12b), for Box-c the 2016/17 peak is weaker than the 2017/18 (Fig. 12c). The Box-d peaks (Fig. 12d) in both winters are more intense than the climatological mean. The occurrence time of Box-e peak (Fig. 12e) in 2016/17 was delayed for about 10 pentads compared with the climatological mean, although the occurrence time of the grid point peaks matches very well with the climatological mean. We will return to the discussion on interannual difference in later part of the paper.

We already see it in Fig. 12 that the occurrence time and the intensity are modulated by the subseasonal variability. The MJO and CCEW influence on the peak events in 2016/2017 and 2017/2018 winters can be further illustrated using the temporal modulation maps of two winters (Fig. 13). The temporal modulation is measured by counting the number of days among the 15 days of the peak event of which the individual type of disturbances is in the convective phase.
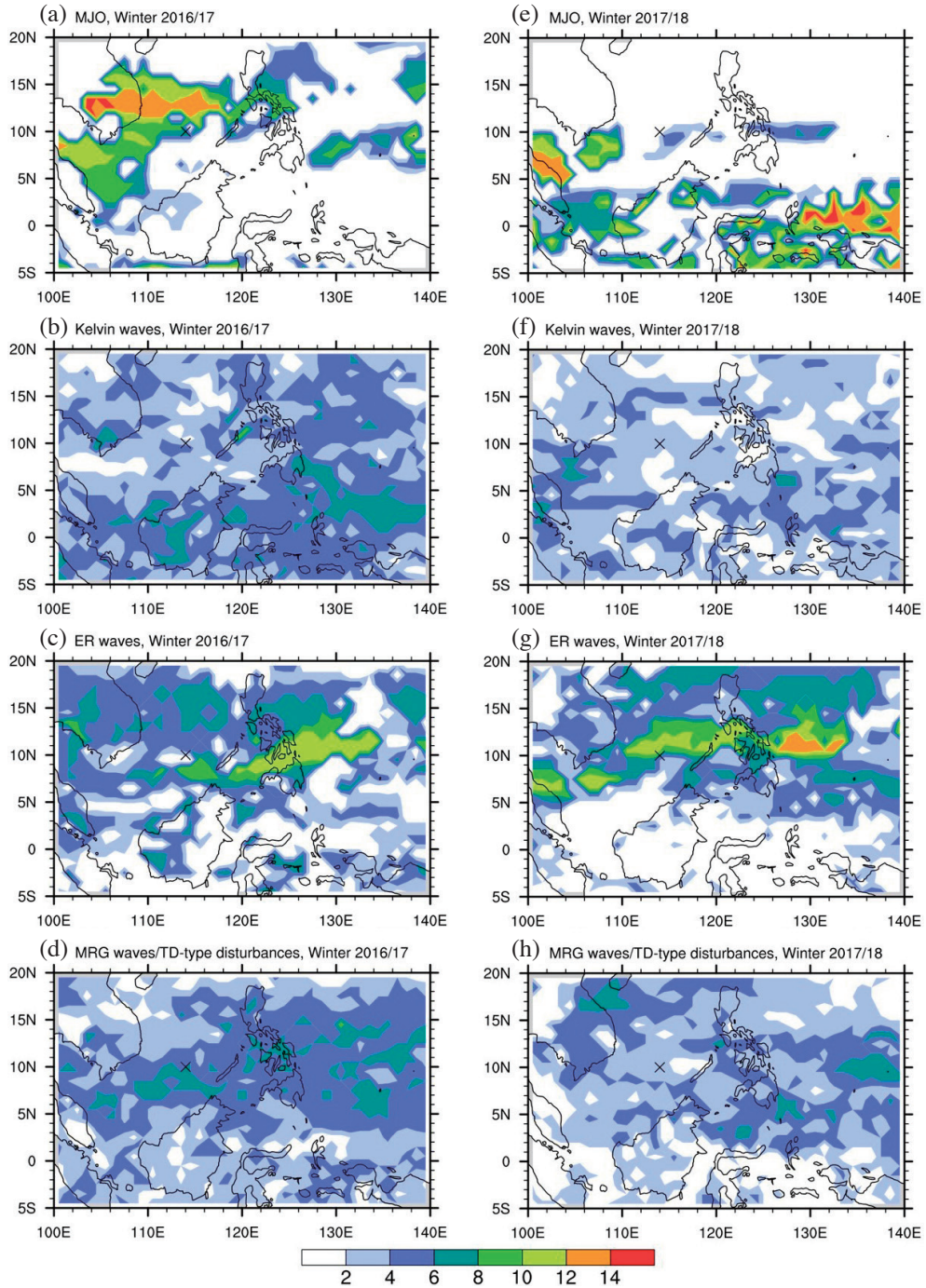
Fig. 13. The number of days with the convective phase of (a) MJO, (b) Kelvin wave, (c) ER wave, and (d) MRG/TD-type disturbance during the 15-day sub-seasonal peak precipitation event in the 2016/17 winter, and (e) - (h) for the sub-seasonal peak precipitation event in the 2017/18 winter.

Figures 13a and c show the MJO influence in 2016/17 is particularly strong for Boxes b - c and the ER influence is strong for Boxes c - d. Figures 13e and g show in 2017/18 the MJO influence is strong for Box-e and the ER influence is strong in Boxes c - d. The temporal modulation of MJO is quite different between these two year. In winter 2016/17, the area of influence is mainly located at SCS, while the main area of influence in winter 2017/18 is at equatorial MC. SCS is almost away from MJO during the peak precipitation period in winter 2017. The contrast may be due to strong northerly wind over the SCS in winter 2017/18 (figure not shown). Besides, the Kelvin and MRG/TD influences in 2016/17 is stronger than in 2017/18, and their contributions are comparable to the climatological mean (Figs. 10b, d). Kelvin waves mainly influence equatorial MC during the peak precipitation event (Figs. 13b, f) and ER and MT (Figs. 13b - d and f - h) influence off-equatorial regions including SCS and Philippine (Boxes c - d, Figs. 13c, d, g, h). The temporal characteristics is also similar to the climatological mean.

The influence of MJO and CCEWs in individual years on the peak events can be clearly seen in the Hovmöller diagrams of daily precipitation in Fig. 14. The dates in the Hovmöller diagrams are determined on the basis of the median and inter-quartile range of the occurrence time of the peak events. The Pentad 0 in each diagram corresponds to the lower quartile of the occurrence time of the peak event at all grid points within each box area of which the longitude boundaries are marked by the light grey lines. The MJO and CCEWs identified based on the procedure described in section 2.2 are indicated in the black (MJO), blue (Kelvin), red (ER), and purple (MRG/TD) with the convective phase in dashed and suppressed phase in solid contours. Overall, we see much busier wave activity in 2016/17 than in 2017/18, while the precipitation intensity in 2017/18 winter is stronger. Box-a (Fig. 14a), which covers Taiwan, is in the subtropical region that shows less influence of the tropical waves compared with other box areas. The peak events in 2016/17 winter are influenced by MRG/TD (Pentad -1 ~ 0 in Fig. 14a, corresponding to 22 November to 1 December) and Kelvin waves (Pentad 2 in Fig. 14a, 2 - 6 December). The Box-a peak events in 2017/18 are weak and show little influence by the waves. The ER modulation can be identified at Pentad 0 (7 - 11 November) in Fig. 14b. The MRG/TD and Kelvin waves modulation despite their weakness can be identified at Pentad 1 and 6, respectively. Figures 14c, e, d, and f present a very interesting contrast between Box-b and Box-c areas during these two winters. Figures 14c and d show precipitation in the Box-b area peak events are more clearly influenced by the eastward propagating waves such as MJO and Kelvin waves than the westward moving waves, although the waves are weak in 2017/18 winter. In contrast to Box-b, peak events in Box-c are more clearly influenced by westward propagating waves. Comparing Figs. 14d and f we find that the eastward

moving disturbances (no specific type of waves was identified) that induced the peak events in Box-b also triggered some rain in Box-c during the Pentad 0 - 1 (17 - 26 December) (Fig. 14f) but much weaker than the rain induced by the westward moving disturbances and ER waves during the Pentad 1 - 4 (22 December to 10 January). It is even more evident in Figs. 14g and h that the westward moving disturbances or waves showed strong influence on the precipitation in Box-d area. On the other hand, Figs. 14i and j show for Box-e both eastward and westward propagating disturbances/waves can modulate strong rainfall in this area. The above results show large geographic difference in the modulation of peak precipitation events by MJO and CCEWs waves. As it was mentioned before that the area-mean Box-e peak in 2016/17 was delayed for about 10 pentads than the climatological mean, although the grid point peaks occurred within the time period very close to the climatological men. Figure 14i shows the scattered occurrence of precipitation events during the entire period of the figure, which is quite a contrast to Fig. 15 which shows the features of area-mean Box-e peak that occurred around the 10th to the 12th Pentad in 2017. Figure 15 shows that the late occurrence of the area-mean peak precipitation over Box-e was resulted from strong Kelvin and ER modulation. For the first area-mean peak event that occurred during Pentad 6 (26 - 30 January) in 2017 a Kelvin wave moved from the Indian Ocean eastward to Box-e area and brought significant amount of rainfall over the entire region. For the second area-mean peak event that occurred during Pentad 10 (15 - 19 February) in 2017 a westward moving ER wave brought significant amount of rainfall over the region that overwhelmed the suppressed phase of the MJO. The ER wave merged with the Kelvin wave over western Indian Ocean and resulted in large rainfall event that persisted from three pentads. The rainfall spatial patterns within Box-e area during these two peak periods are similar, while the first peak saw active precipitation over the equatorial belt from 10°S to 5°N but the second peak saw active precipitation over 5 - 10°N over the Philippine Sea. The large area precipitation is clearly associated with the CCEWs.

6. SUMMARY AND CONCLUDING REMARKS

We have shown that the precipitation over the SCS-MC region during the wet period (November to February) of the boreal winter half year has distinct temporal and regional characteristics associated with the seasonal cycle. A new term "sub-seasonal peak precipitation event" is introduced in this study in order to focus the analysis on providing useful observational evidence to assist S2S prediction. Using the cases in the SCSTIMX winters we have demonstrated that the peak precipitation events at each grid as well as computed as an area-mean can be influenced differently by MJO and CCEWs. Although MJO and CCEWs can
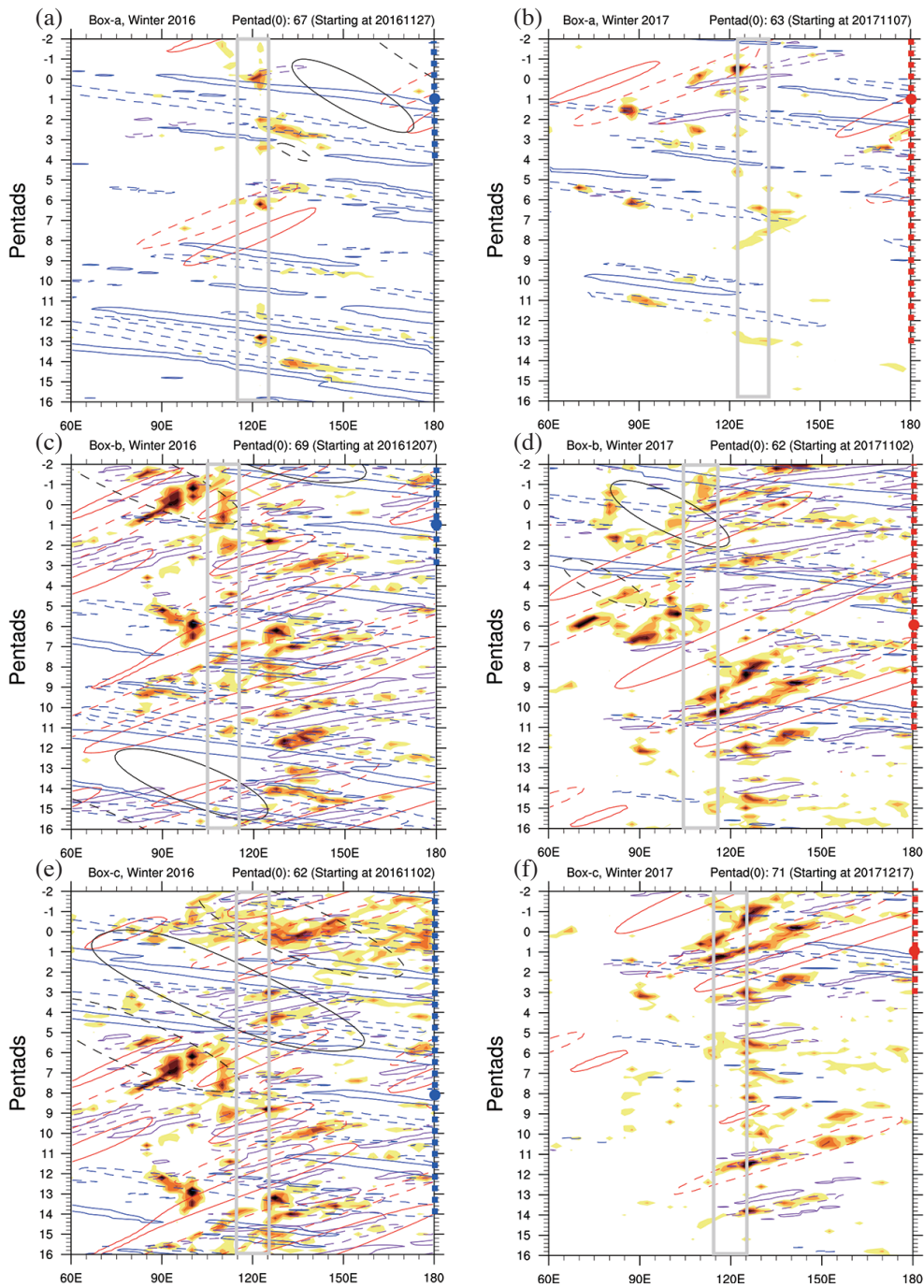
Fig. 14. Hovmöller diagram of daily precipitation (mm day^{-1}, shaded) and the MJO (black contours), Kelvin wave (blue contours), ER wave (red contours), and MRG/TD-type disturbance (purple contours) determined based on the filtered OLR (unit: W m^{-2}). Only the days relevant to the subseasonal peak precipitation event are plotted. (a) (c) (e) (g) (i) show the evens at Boxes a - e during the 2016/17 winter and (b) (d) (f) (h) (j) show the events at Boxes a - e during the 2017/18 winter. The median time and inter-quartile range of the peak events, the same as what is shown in Fig. 12, are marked on the right boundary of the figures with Pentad number -2 corresponding to the time of lower quartile. The longitudinal range of each sub-area is marked by the grey box to highlight the location where the peak events are identified. Contour levels are according to the wave activity thresholds listed in Table 1. Solid contours represent suppressed phase and dashed lines are convective phase.
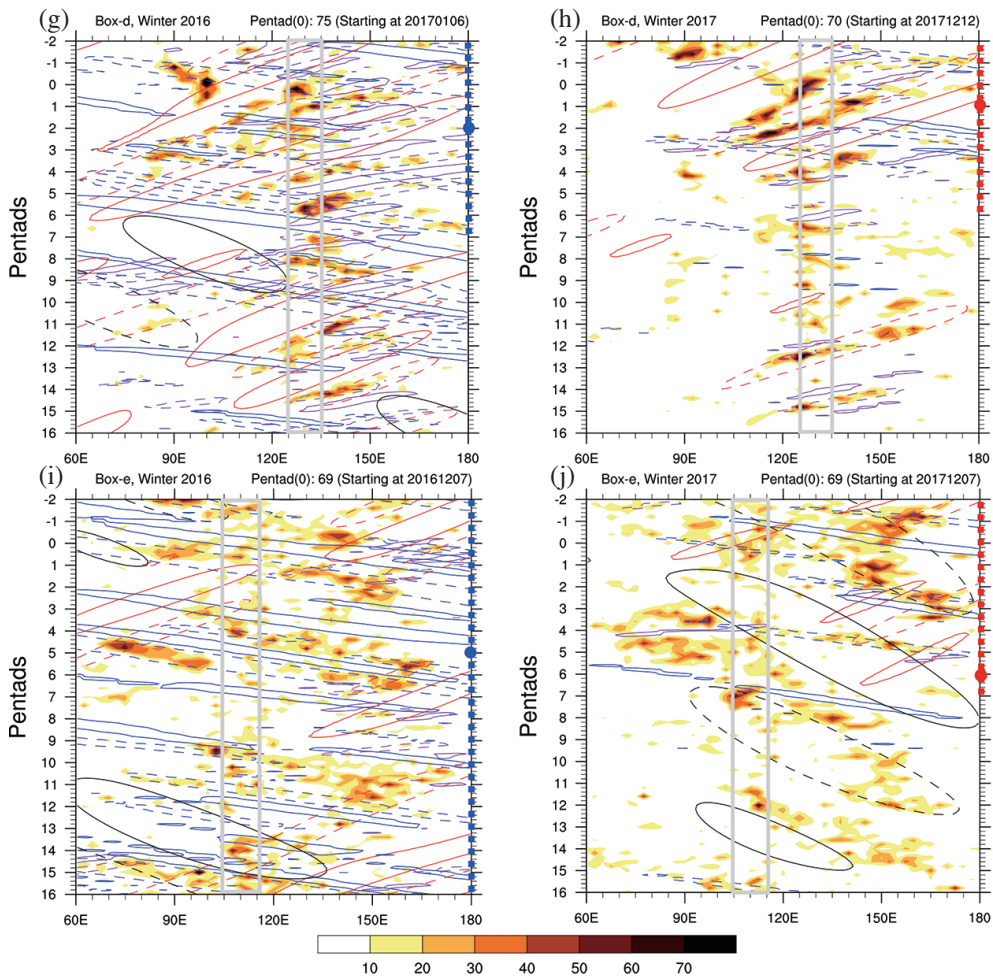
Fig. 14. (Continued)
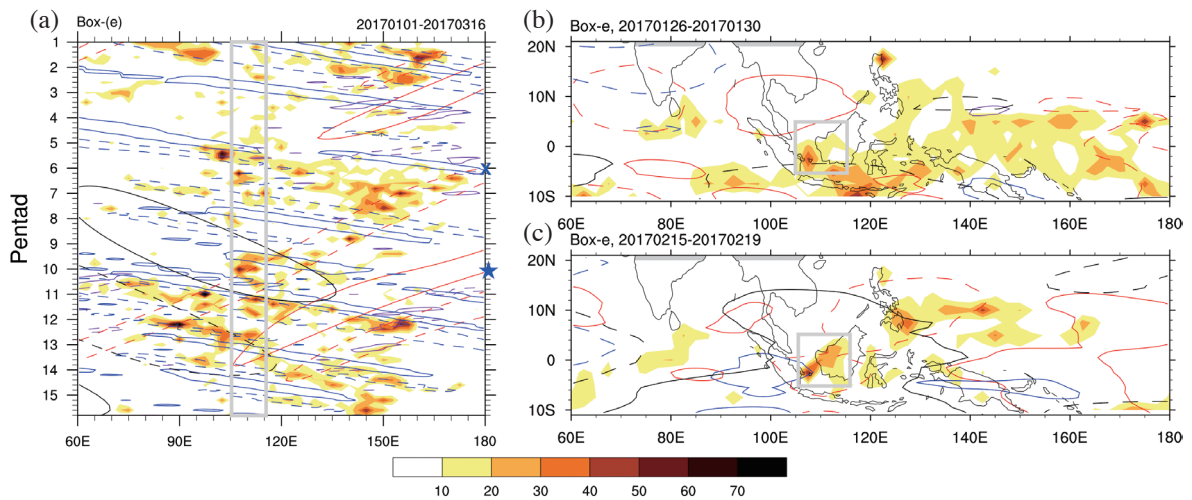

Fig. 15. (a) Similar to Fig. 14 but for the period from 1 January to 16 March in 2017. Two peaks of the area mean precipitation shown in Fig. 12e (blue line) are marked on the right boundary. The geographical distribution of the precipitation and CCEWs averaged over the time are presented in (b) for the first peak (26 - 30 January 2017) and (c) for the second peak (15 - 19 February 2017).

influence the timing and intensity of the peak precipitation, the seasonal cycle and topography effects are important to the local peak event. Also, large geographical difference within the SCS-MC region is observed. The precipitation intensity during the 2017/18 peak event on average is stronger than normal, especially over central SCS (Boxes b - d), the Philippines and the western Philippine Sea areas, which is resulted from the strong modulation of the ER wave. The peak precipitation over Box-e (western Borneo and the SCS between Sumatra and Borneo) in 2016/17 winter was modulated by MJO and three types of CCEWs, while the winter maximum of the summed precipitation over entire Box-e area was delayed for three weeks compared with the climatology. Convection over Box-e was enhanced by Kelvin waves (Fig. 14i). However, the area-mean rainfall peak was delayed until a large area of the convection is enhanced by the Kelvin and ER waves (Fig. 15). Our findings in this study suggests the importance of understanding the MJO and CCEW modulation on the SCS-MC precipitation to improve S2S prediction in the region.

It is worth noting that the mean precipitation intensity averaged over the days with convective CCEWs is stronger than the intensity without the modulation. Therefore, even for short-range weather forecast, accurately predict the waves is important for precipitation prediction.

The dynamic process associated with CCEWs and its influence on precipitation has been studied by many authors. Roundy and Frank (2004) analysed OLR and precipitable water (PW) data and found that the CCEW modes control much of the variance of tropical convection, suppressing or enhancing regional convection. Precipitable water associated with ER, MRG, and TD-type waves or disturbances also produce meridional advection across regions of strong PW gradients. Tulich and Kiladis (2012) used a WRF model and satellite rainfall data to study the coupling process of convection and inertio-gravity-wave and documented its importance in the context of mesoscale squall lines. Yasunaga and Mapes (2012) explored the modulations of convective versus stratiform rain, rain system size, and column water vapor by CCEWs based on multiyear satellite data. They found Kelvin and inertia-gravity waves have strong influence on mesoscale convection systems (MCSs) accompanied with stratiform rain, while the more rotational ER, MRG, and TD-type waves or disturbances show strong modulation on scattered convection. MJOs have the unique characteristics of both rotational and divergent component, which modulate stratiform rainfall and smaller-sized precipitation features, convective rainfall. From column water vapor composites, they also found that the more rotational wave types modulate the moisture field more than do the more divergent waves.

Other than the dynamic processes, the diurnal cycle and waves interaction is also a crucial influential factor on precipitation. Most studies examine the modulation of diurnal cycle by MJO. The mean diurnal amplitude of land precipitation is enhanced ahead of the MJO convection envelope, while the precipitation over the coastal ocean is largely suppressed (e.g., Peatman et al. 2014; Hung and Sui 2018). Chen et al. (2019) analysed the convectively active Kelvin waves during December 2016 and revealed that the diurnal cycle hotspots over the land were modulated depending on the background wind and terrain effects, and the enhanced coastal convection organizations were found in specific coastal areas. It is beyond the scope of the current study to carry out detailed analysis or simulation of the dynamic process associated with CCEWs and its influence on precipitation variability. More research is needed in this direction for improving our understanding on S2S prediction model capability and predictability. The analysis procedure presented in this paper can be used in real-time precipitation, MJO and CCEWs monitoring and S2S model prediction verification over the SCS-MC region.

REFERENCES

Berrisford, P., D. P. Dee, P. Poli, R. Brugge, M. Fielding, M. Fuentes, P. W. Kållberg, S. Kobayashi, S. Uppala, and A. Simmons, 2011: The ERA-Interim Archive Version 2.0, ERA Report Series, ECMWF, Shinfield Park, Reading.

Chang, C.-P., Z. Wang, J. Ju, and T. Li, 2004: On the relationship between western Maritime Continent monsoon rainfall and ENSO during northern winter. *J. Clim.*, **17**, 665-672, doi: 10.1175/1520-0442(2004)017<0665:otrbwm>2.0.co;2. [Link]

Chang, C.-P., P. A. Harr, and H.-J. Chen, 2005a: Synoptic disturbances over the equatorial South China Sea and western Maritime Continent during boreal winter. *Mon. Weather Rev.*, **133**, 489-503, doi: 10.1175/MWR-2868.1. [Link]

Chang, C.-P., Z. Wang, J. McBride, and C.-H. Liu, 2005b: Annual cycle of Southeast Asia—Maritime Continent rainfall and the asymmetric monsoon transition. *J. Clim.*, **18**, 287-301, doi: 10.1175/JCLI-3257.1. [Link]

Chen, J.-M., C.-H. Tsou, R. Wu, and C.-H. Sui, 2020: Introduction to the special issue on South China Sea Two-Island Monsoon Experiment (SCSTIMX): Observation, simulation, and projection. *Terr. Atmos. Ocean. Sci.*, **31**, 97-101, doi: 10.3319/TAO.2020.03.19.01. [Link]

Chen, T.-C., J.-D. Tsay, J. Matsumoto, and J. Alpert, 2015a: Development and formation mechanism of the Southeast Asian winter heavy rainfall events around the South China Sea. Part I: Formation and propagation

of cold surge vortex. *J. Clim*., **28**, 1417-1443, doi: 10.1175/JCLI-D-14-00170.1. [Link]

Chen, T.-C., J.-D. Tsay, and J. Matsumoto, 2015b: Development and formation mechanism of the Southeast Asian winter heavy rainfall events around the South China Sea. Part II: Multiple interactions. *J. Clim*., **28**, 1444-1464, doi: 10.1175/JCLI-D-14-00171.1. [Link]

Chen, W.-T., S.-P. Hsu, Y.-H. Tsai, and C.-H. Sui, 2019: The Influences of Convectively Coupled Kelvin Waves on Multiscale Rainfall Variability over the South China Sea and Maritime Continent in December 2016. *J. Clim*., **32**, 6977-6993, doi: 10.1175/jcli-d-18-0471.1. [Link]

Frank, W. M. and P. E. Roundy, 2006: The Role of Tropical Waves in Tropical Cyclogenesis. *Mon. Weather Rev*., **134**, 2397-2417, doi: 10.1175/MWR3204.1. [Link]

Funk, C., P. Peterson, M. Landsfeld, D. Pedreros, J. Verdin, S. Shukla, G. Husak, J. Rowland, L. Harrison, A. Hoell, and J. Michaelsen, 2015: The climate hazards infrared precipitation with stations—A new environmental record for monitoring extremes. *Sci. Data*, **2**, 150066, doi: 10.1038/sdata.2015.66. [Link]

Haylock, M. and J. McBride, 2001: Spatial coherence and predictability of Indonesian wet season rainfall. *J. Clim*., **14**, 3882-3887, doi: 10.1175/1520-0442(2001)014<3882:scapoi>2.0.co;2. [Link]

Hung, C.-S. and C.-H. Sui, 2018: A diagnostic study of the evolution of the MJO from Indian Ocean to Maritime Continent: Wave dynamics versus advective moistening processes. *J. Clim*., **31**, 4095-4115, doi: 10.1175/JCLI-D-17-0139.1. [Link]

Hung, C.-W. and M. Yanai, 2004: Factors contributing to the onset of the Australian summer monsoon. *Q. J. R. Meteorol. Soc*., **130**, 739-758, doi: 10.1256/qj.02.191. [Link]

Johnson, R. H. and R. A. Houze, 1987: Precipitating cloud systems of the Asian monsoon. In: Chang, C.-P. and T. N. Krishnamurti (Eds.), Monsoon Meteorology, Oxford University Press, New York, 298-353.

Joyce, R. J., J. E. Janowiak, P. A. Arkin, and P. Xie, 2004: CMORPH: A Method that Produces Global Precipitation Estimates from Passive Microwave and Infrared Data at High Spatial and Temporal Resolution. *J. Hydrometeorol*., **5**, 487-503, doi: 10.1175/1525-7541(2004)005<0487:CAMTPG>2.0.CO;2. [Link]

Kikuchi, K. and B. Wang, 2008: Diurnal Precipitation Regimes in the Global Tropics. *J. Clim*., **21**, 2680-2696, doi: 10.1175/2007JCLI2051.1. [Link]

Kiladis, G. N., M. C. Wheeler, P. T. Haertel, K. H. Straub, and P. E. Roundy, 2009: Convectively coupled equatorial waves. *Rev. Geophys*., **47**, doi: 10.1029/2008RG000266. [Link]

Kiladis, G. N., J. Dias, K. H. Straub, M. C. Wheeler, S. N. Tulich, K. Kikuchi, K. M. Weickmann, and M. J. Ventrice, 2014: A comparison of OLR and circulation-based indices for tracking the MJO. *Mon. Weather Rev*., **142**, 1697-1715, doi: 10.1175/MWR-D-13-00301.1. [Link]

Kim, H., F. Vitart, and D. E. Waliser, 2018: Prediction of the Madden-Julian Oscillation: A Review. *J. Clim*., **31**, 9425-9443, doi: 10.1175/JCLI-D-18-0210.1. [Link]

Kuo, K.-T., W.-T. Chen, and C.-M. Wu, 2020: Effects of convection-SST interactions on the South China Sea summer monsoon onset in a multiscale modeling framework model. *Terr. Atmos. Ocean. Sci*., **31**, 211-225, doi: 10.3319/TAO.2019.08.16.01. [Link]

Lee, H.-T., 2011: NOAA Climate Data Record (CDR) of Daily Outgoing Longwave Radiation (OLR), Version 1.2, NOAA National Climatic Data Center, doi: 10.7289/V5SJ1HH2. [Link]

Liebmann, B. and H. H. Hendon, 1990: Synoptic-scale disturbances near the equator. *J. Atmos. Sci*., **47**, 1463-1479, doi: 10.1175/1520-0469(1990)047<1463:ssdnte>2.0.co;2. [Link]

Lim, S. Y., C. Marzin, P. Xavier, C.-P. Chang, and B. Timbal, 2017: Impacts of boreal winter monsoon cold surges and the interaction with MJO on Southeast Asia rainfall. *J. Clim*., **30**, 4267-4281, doi: 10.1175/JCLI-D-16-0546.1. [Link]

Ling, J., C. Li, T. Li, X. Jia, B. Khouider, E. Maloney, F. Vitart, Z. Xiao, and C. Zhang, 2017: Challenges and Opportunities in MJO Studies. *Bull. Amer. Meteorol. Soc*., **98**, ES53-ES56, doi: 10.1175/BAMS-D-16-0283.1. [Link]

Lu, M.-M., C.-H. Sui, J.-R. Sun, and P.-H. Lin, 2020: Influences of subseasonal to interannual oscillations on the SCS summer monsoon onset in 2018. *Terr. Atmos. Ocean. Sci*., **31**, 197-209, doi: 10.3319/TAO.2020.02.25.01. [Link]

Lubis, S. W. and C. Jacobi, 2015: The modulating influence of convectively coupled equatorial waves (CCEWs) on the variability of tropical precipitation. *Int. J. Climatol*., **35**, 1465-1483, doi: 10.1002/joc.4069. [Link]

Matsuno, T., 1966: Quasi-Geostrophic Motions in the Equatorial Area. *J. Meteorol. Soc. Jpn*., **44**, 25-43, doi: 10.2151/jmsj1965.44.1_25. [Link]

McBride, J. L., M. R. Haylock, and N. Nicholls, 2003: Relationships between the Maritime Continent heat source and the El Niño-Southern Oscillation phenomenon. *J. Clim*., **16**, 2905-2914, doi: 10.1175/1520-0442(2003)016<2905:rbtmch>2.0.co;2. [Link]

Moron, V., A. W. Robertson, and J.-H. Qian, 2010: Local versus regional-scale characteristics of monsoon onset and post-onset rainfall over Indonesia. *Climate Dyn*., **34**, 281-299, doi: 10.1007/s00382-009-0547-2. [Link]

Nguyen, D.-Q., J. Renwick, and J. McGregor, 2016: On the presence of tropical vortices over the Southeast Asian sea–Maritime Continent region. *J. Clim.*, **29**, 4793-4800, doi: 10.1175/JCLI-D-14-00468.1. [Link]

Peatman, S. C., A. J. Matthews, and D. P. Stevens, 2014: Propagation of the Madden-Julian Oscillation through the Maritime Continent and scale interaction with the diurnal cycle of precipitation. *Q. J. R. Meteorol. Soc.*, **140**, 814-825, doi: 10.1002/qj.2161. [Link]

Qian, J.-H., 2008: Why precipitation is mostly concentrated over islands in the Maritime Continent. *J. Atmos. Sci.*, **65**, 1428-1441, doi: 10.1175/2007JAS2422.1. [Link]

Qian, J.-H., A. W. Robertson, and V. Moron, 2013: Diurnal cycle in different weather regimes and rainfall variability over Borneo associated with ENSO. *J. Clim.*, **26**, 1772-1790, doi: 10.1175/JCLI-D-12-00178.1. [Link]

Robertson, A. W., V. Moron, J.-H. Qian, C.-P. Chang, F. Tangang, E. Aldrian, T. Y. Koh, and J. Liew, 2011: The Maritime Continent monsoon. In: Chang, C.-P., Y. Ding, N.-C. Lau, R. H. Johnson, B. Wang, and T. Yasunari (Eds.), The Global Monsoon System: Research and Forecast, World Scientific Series on Asia-Pacific Weather and Climate: Volume 5, World Scientific, 85-98, doi: 10.1142/9789814343411_0006. [Link]

Roundy, P. E. and W. M. Frank, 2004: A Climatology of Waves in the Equatorial Region. *J. Atmos. Sci.*, **61**, 2105-2132, doi: 10.1175/1520-0469(2004)061<2105:ACOWIT>2.0.CO;2. [Link]

Schlueter, A., A. H. Fink, P. Knippertz, and P. Vogel, 2019: A Systematic Comparison of Tropical Waves over Northern Africa. Part I: Influence on Rainfall. *J. Clim.*, **32**, 1501-1523, doi: 10.1175/JCLI-D-18-0173.1. [Link]

Stan, C., D. M. Straus, J. S. Frederiksen, H. Lin, E. D. Maloney, and C. Schumacher, 2017: Review of Tropical-Extratropical Teleconnections on Intraseasonal Time Scales. *Rev. Geophys.*, **55**, 902-937, doi: 10.1002/2016RG000538. [Link]

Sui, C.-H., P.-H. Lin, W.-T. Chen, S. Jan, C.-Y. Liu, Y.-J. Yang, C.-H. Liu, J.-M. Chen, M.-J. Yang, J.-S. Hong, L.-H. Hsu, and L.-S. Tseng, 2020: The South China Sea Two Islands Monsoon Experiment for studying convection and subseasonal to seasonal variability. *Terr. Atmos. Ocean. Sci.*, **31**, 103-129, doi: 10.3319/TAO.2019.11.29.02. [Link]

Tangang, F. T., L. Juneng, E. Salimun, P. N. Vinayachandran, Y. K. Seng, C. J. C. Reason, S. K. Behera, and T. Yasunari, 2008: On the roles of the northeast cold surge, the Borneo vortex, the Madden-Julian oscillation, and the Indian Ocean dipole during the extreme 2006/2007 flood in southern peninsular Malaysia. *Geophys. Res. Lett.*, **35**, L14S07, doi: 10.1029/2008GL033429. [Link]

Tulich, S. N. and G. N. Kiladis, 2012: Squall Lines and Convectively Coupled Gravity Waves in the Tropics: Why Do Most Cloud Systems Propagate Westward? *J. Atmos. Sci.*, **69**, 2995-3012, doi: 10.1175/JAS-D-11-0297.1. [Link]

Van der Linden, R., A. H. Fink, J. G. Pinto, T. Phan-Van, and G. N. Kiladis, 2016: Modulation of Daily Rainfall in Southern Vietnam by the Madden-Julian Oscillation and Convectively Coupled Equatorial Waves. *J. Clim.*, **29**, 5801-5820, doi: 10.1175/JCLI-D-15-0911.1. [Link]

Vincent, C. L. and T. P. Lane, 2016: Evolution of the diurnal precipitation cycle with the passage of a Madden-Julian oscillation event through the Maritime Continent. *Mon. Weather Rev.*, **144**, 1983-2005, doi: 10.1175/MWR-D-15-0326.1. [Link]

Vitart, F. and A. W. Robertson, 2019: Chapter 1 - Introduction: Why Sub-seasonal to Seasonal Prediction (S2S)? In: Robertson, A. W. and F. Vitart (Eds.), Sub-Seasonal to Seasonal Prediction: The Gap Between Weather and Climate Forecasting, Elsevier, 3-15, doi: 10.1016/b978-0-12-811714-9.00001-2. [Link]

Wheeler, M. and G. N. Kiladis, 1999: Convectively Coupled Equatorial Waves: Analysis of Clouds and Temperature in the Wavenumber-Frequency Domain. *J. Atmos. Sci.*, **56**, 374-399, doi: 10.1175/1520-0469(1999)056<0374:CCEWAO>2.0.CO;2. [Link]

Wheeler, M. C. and H. H. Hendon, 2004: An All-Season Real-Time Multivariate MJO Index: Development of an Index for Monitoring and Prediction. *Mon. Weather Rev.*, **132**, 1917-1932, doi: 10.1175/1520-0493(2004)132<1917:AARMMI>2.0.CO;2. [Link]

Woolnough, S. J., 2019: Chapter 5 - The Madden-Julian Oscillation. In: Robertson, A. W. and F. Vitart (Eds.), Sub-Seasonal to Seasonal Prediction: The Gap Between Weather and Climate Forecasting, Elsevier, 93-117, doi: 10.1016/B978-0-12-811714-9.00005-X. [Link]

Xie, P., R. Joyce, S. Wu, S.-H. Yoo, Y. Yarosh, F. Sun, and R. Lin, 2017: Reprocessed, Bias-Corrected CMORPH Global High-Resolution Precipitation Estimates from 1998. *J. Hydrometeorol.*, **18**, 1617-1641, doi: 10.1175/JHM-D-16-0168.1. [Link]

Yang, G.-Y. and J. Slingo, 2001: The diurnal cycle in the tropics. *Mon. Weather Rev.*, **129**, 784-801, doi: 10.1175/1520-0493(2001)129<0784:tdcitt>2.0.co;2. [Link]

Yasunaga, K. and B. Mapes, 2012: Differences between More Divergent and More Rotational Types of Convectively Coupled Equatorial Waves. Part II: Composite Analysis based on Space-Time Filtering. *J. Atmos. Sci.*, **69**, 17-34, doi: 10.1175/JAS-D-11-034.1. [Link]

Yatagai, A., K. Kamiguchi, O. Arakawa, A. Hamada, N. Yasutomi, and A. Kitoh, 2012: APHRODITE: Constructing a long-term daily gridded precipitation dataset for Asia based on a dense network of rain gauges. *Bull. Amer. Meteorol. Soc.*, **93**, 1401-1415, doi: 10.1175/BAMS-D-11-00122.1. [Link]